

Numerical Analysis of Flow and Mass Transfer in Humid Fractal Surfaces

T. Cardoso de Souza, S. J. F. Erich

Department of Applied Physics, Eindhoven University of Technology
Den Dolech 2, 5612 AZ, Eindhoven, The Netherlands
t.cardoso.de.souza@tue.nl; S.J.F.Erich@tue.nl

Abstract - In this paper we investigate the convective mass transfer process between a laminar air flow passing over a humid fractal surface. To determine the mass transfer convection coefficient, h_m , in complex ‘wetted’ fractal geometries, a simple numerical method is considered to obtain the rate of evaporation for any type of surface. This approach is validated considering two benchmark cases commonly discussed in laminar boundary layer theory, e.g., the flow over a flat plate and the flow over a cylinder. By considering different types of fractal geometries and different air flow speeds, we characterize the effects that such multi-scale fractals have on the convective mass transport driving the surface averaged rate of evaporation, \bar{n}_A . The results show the potential of fractals surfaces to enhance evaporation, where depending on the fractal shape considered, for instance, an increase by more than a factor of 3 in the rate of evaporation was obtained in comparison with a reference case where no fractals structures are imposed.

Keywords: Multi-scale fractal forcing, evaporation enhancement, laminar flows

1. Introduction

To date, research on the use of complex shaped surfaces and their interaction with a fluid flow blowing over or through them has been considered within a variety of applications ranging from skating sports [1], combustion improvement [2, 3] up to acoustics noise reduction in airplane wings [4]. While most cases are associated with turbulent flows, where by agitating the chaotic motions of the flow over a substantial range of spatial and time scales, i.e., the so-called multi-scale forcing, a significant alteration in the mixing capabilities, for instance, could be reached [5], in this paper we consider the application of fractals surfaces in combination with a laminar air flow, at relatively low speed, to enhance evaporation in situations where convective evaporative cooling is a relevant factor to consider. In fact, fractals surfaces are pertinent for these type of applications since the inherent self-similarity property of these objects [6, 7] is capable of generating a large surface to volume ratio, a property which is particularly relevant if one wants to enhance the rate of evaporation through the increase of the surface area within a small volume space region. Taking this in consideration, the purpose of this paper is to discuss the interrelated aspects of the boundary layer and the convective mass transfer associated with a laminar air flow passing over a humid fractal surface. The focus relies on the relation between the free flow and the evaporation mass transfer that takes place within the boundary layer flow formed along the fractal surface. Here we investigate numerically whether by introducing such fractals the enhancement of the convective mass transfer might be achieved. Our main strategy consists in the application of fractals, acting as a “passive forcing stirrer”, to disturb the free flow while enhancing the evaporation transport between the humid surface and the laminar air flow. The goal is to show that fractal objects are specially suited for applications requiring the improvement of convective evaporation.

In this paper, the analysis of the physics coupling between the laminar air flow and the momentum and concentration boundary layer formed at the fractal surface is carried out considering a relatively simple 2D numerical model that accounts for the evaporation effects and the subsequent increasing of the moisture concentration in the surrounding air flow. In this model, the laminar flow is initially dryer than the humid surface. By applying a fractal geometry at the surface it is expected that an enhancement of the water vapor flux between the “wetted” surface and the air environment surrounding it could be established in connection with the type of the fractal geometry applied over the surface. We consider two types of fractal geometries, namely the so-called *Von Koch* fractal set, also referred as the *Koch* snowflake, and the *Sierpinski* curve with fractal motifs resembling an arrowhead [6]. Since the arrowhead fractal geometry generates a

larger surface area than the Koch-type fractals, these fragmented shape objects are expected to enhance significantly the rate of evaporation of the humid surface.

The organization of this paper is as follows. In section 2 we describe in detail the numerical model used in these simulations, namely the numerical parameters, the boundary conditions and the different types of fractal surfaces considered in this investigation. Subsequently, the evaporation model will be presented in section 3 and its validation considered in terms of two simple benchmark cases, e.g., the flow over a flat plate and the flow over a cylinder. The discussion of the results is presented in section 4 for the reference case, i.e., the solid surface without fractals imposed, and for the cases with the fractals applied. Conclusion remarks are contained in section 5.

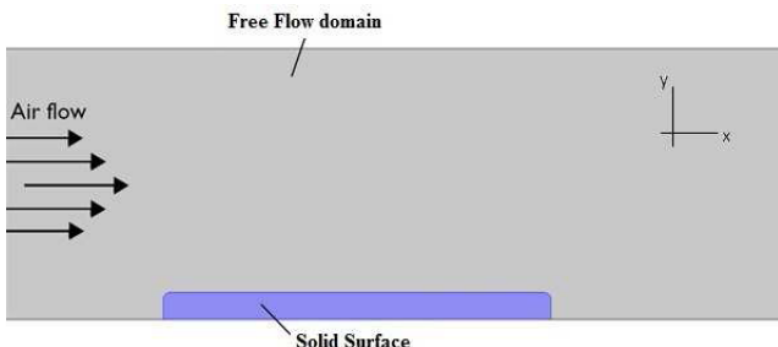


Fig. 1: 2D view of the computational domain showing the different regions for the reference case, i.e., no fractals imposed along the solid surface. The size of the free flow domain is $10 \text{ mm} \times 50 \text{ mm}$, while the solid surface domain has the dimensions: $1 \text{ mm} \times 15 \text{ mm}$.

2. Numerical Model

In these simulations, the system of Navier-Stokes equations and the scalar transport are solved in a two-dimensional 2D numerical domain with the *COMSOL* 5.1 solver. The analysis of the laminar air flow and the mass transport over the humid surface is considered through the numerical domain shown in Fig. 1.

In these simulations, we investigate the coupling effects due to the rate of evaporation and the boundary layer for a laminar dry air flow imposed at the inlet with velocities varying within the range $10 \text{ cm/s} \leq U_{air} \leq 1.5 \text{ m/s}$. A material library database in *COMSOL* including thermal-physical properties for air at temperature $T = 25^\circ\text{C}$ is used. In these simulations the increase of the moisture content in the air flow is not considered to provide changes in its physical properties.

Boundary conditions used in these simulations are defined as follows. At the inlet, a laminar dry air flow with velocity U_{air} is imposed while at the outlet for each velocity component u_i and the scalar specie c , i.e., water vapor concentration, Neumann boundary conditions are applied. Pressure is hold constant at the outlet and equal to the atmospheric pressure. In the solid surface, a thin film with water vapor concentration at saturated conditions is imposed as Dirichlet boundary condition. Closely following [8], it is assumed that the air just above the surface is in thermodynamical equilibrium with the water vapor concentration at the surface, which is in turn related with the saturation vapor pressure through the ideal gas law:

$$c_{sat}(T_s) = \frac{p_{sat}(T_s)}{RT_s} \quad (1)$$

where p_{sat} is the water vapor saturation pressure determined using the Clausius–Clapeyron relation, $T_s = 25^\circ\text{C}$ is the temperature of the solid surface and $c_{sat} [\text{mol/m}^3]$ is the moisture saturation concentration at the surface. Considering the type of fractal geometry imposed over the solid surface, in this paper we restrict to fractal geometries of *Koch*-type and *arrow*-type as already mentioned. These fractal objects are illustrated in Figs. 2-3. In these numerical simulations, for both *Koch* and *arrow*-type geometries we set the generation of the fractal surfaces up to a maximum of four iterations. The main reason to limit the fractality of the surfaces to such iterative level is mostly due to practical purposes. In fact, the ever decreasing size of the fractal motifs, arising from the fractal similarity as the number of iterations to generate the corresponding structures increases, requires meshes with higher spatial resolutions that quickly become difficult to be

treated using finite element methods, especially when the interface between the solid surface and the air domain is resolved using additional extra layers, e.g., boundary layers.

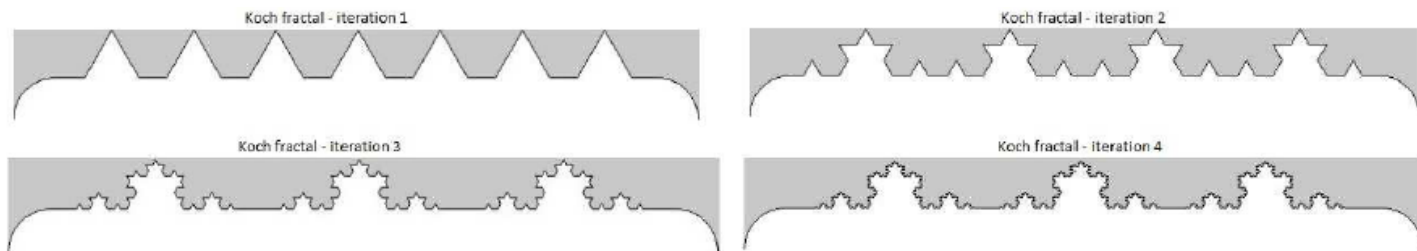


Fig. 2: Solid domain with fractal surfaces of *Koch*-type geometry. We only consider the developing of fractal *Koch*-surfaces obtained up to four iterative procedures.

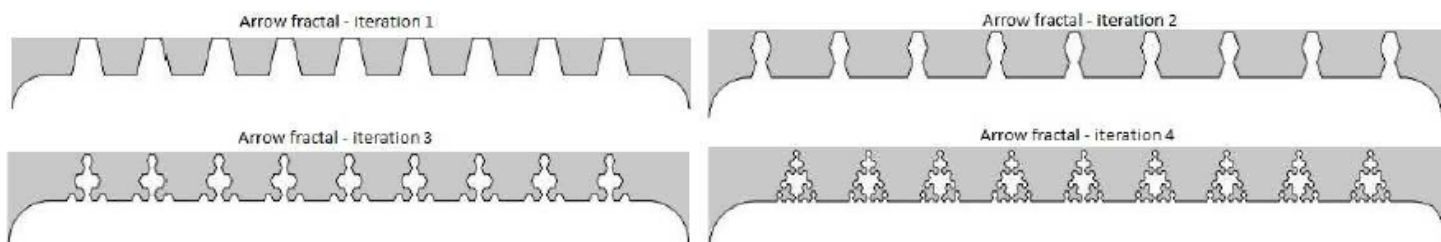


Fig. 3: Solid domain with fractal surfaces of *arrow*-type geometry. Also, only fractal *arrow*-surfaces obtained up to four iterative procedures are used.

Next we introduce the evaporation model used in these simulations.

3. Evaporation Model

One of the main challenges associated with convective mass transfer concerns to the absence of analytical or empirical expressions to predict and to describe the mass transfer flux between humid solid surfaces of complex shapes, which has a boundary layer concentration attached to it, and the external air flow. One reason for such difficulties is due to the advection motion of the fluid layers within the boundary layer which depends on local conditions associated with the geometry of the surface under consideration. However, for some simple cases such as the flow over a flat plate or the flow over a cylinder analytical expressions for the convective mass transfer, h_m , are available, thus allowing to assess the surface averaged rate of evaporation, \bar{n}_A , along the surface of these geometries. In such cases, analytical expressions are directly obtained by solving the system of boundary layer equations with a specified set of boundary conditions [8].

In many applications concerning convective mass-heat transfer, the so-called heat-mass transfer analogy, based on the similarity between the boundary layer equations for the energy and the scalar concentration, is often used. This simplified assumption is evoked under situations involving forced convection flows at relatively low speeds [8]. Using the heat-mass transfer analogy an expression relating the averaged dimensionless mass transfer coefficient \overline{Sh} , i.e., the Sherwood number, and the dimensionless heat transfer coefficient, i.e., the Nusselt number, \overline{Nu} , can be obtained [8]. Following this procedure, in this paper we use this assumption to obtain the mass transfer convection coefficient, h_m , from the analogy between the dimensionless parameters \overline{Sh} , and \overline{Nu} . In more detail, if we consider a laminar flow of dry air over a flat plate with a thin film of water on it, the convective evaporation rate at the surface is determined using the following expression [8]:

$$\bar{n}_A = \bar{h}_m c_{sat} (T_s) \quad (2)$$

where \bar{n}_A is the surface averaged rate of evaporation in $\frac{mol}{m^2s}$ of the water vapour concentration at the surface, \bar{h}_m is the surface averaged convective mass transfer coefficient in $[m/s]$ and $c_{sat}(T_s)$ is the saturated concentration $\frac{mol}{m^3}$ of water vapor at temperature T_s given by (1).

Using the mass-heat transfer analogy for the flat plate and for the cylinder case an expression for the surface averaged dimensionless mass transfer coefficient, \overline{Sh} , is promptly determined from the available expressions of \overline{Nu} , which are in turn obtained by solving the set of energy-momentum boundary layer equations, with given set of boundary conditions, at the corresponding surfaces. More details are found in [8], here we directly refer to the dimensionless parameter \overline{Sh} as given by:

$$\overline{Sh} = C \left(Re^{1/2} \right) \left(Sc^{1/3} \right), \quad (3)$$

where C is a constant that depends on the geometry under consideration and it is equal to $C = 0.332$ for the flat plate geometry and $C = 1.15$ for the cylinder case, Re is the Reynolds number and $Sc = \nu/D_w$ is the Schmidt number. The coefficient D_w is the water vapor diffusion coefficient into air at temperature T_s . From relation 3 the surface averaged mass transfer coefficient \bar{h}_m can then be obtained from its definition:

$$\bar{h}_m = D_w \frac{\overline{Sh}}{L}, \quad (4)$$

where L is a characteristic length of the flow, e.g., for the flat plate L is its length while for the flow over the cylinder it is the diameter of the cylinder. Note that for the cylinder case the relation given by (3) is valid only at the stagnation point in front of the cylinder [8].

Unfortunately, for the specific set of fractal surfaces considered in this paper there are no empirical or analytical expressions for the dimensionless mass transfer convection coefficient \overline{Sh} , as given by relation 3 for the flat plate and for the cylinder case, which allows one to obtain \bar{h}_m and thereby the evaporation, \bar{n}_A , on a surface with a specified water vapour concentration over it. To overcome such difficulty, we determine the rate of evaporation, n_A , by locally assessing the water vapor concentration gradient, which develops between the humid saturated surface and the laminar flow, throughout the complex shaped surface using Fick's law of diffusion:

$$n_A = -D_w \frac{\partial c_A}{\partial y} \Big|_{y=0}, \quad (5)$$

where $\frac{\partial c_A}{\partial y}$ is evaluated locally along the wall surface, i.e., $y=0$, using *COMSOL*. Subsequently, the averaged rate of evaporation \bar{n}_A is computed by spatially averaging the local rate of evaporation n_A along the entire 'humid' surface using the following expression:

$$\bar{n}_A = \frac{1}{L} \int n_A dl, \quad (6)$$

In the next section we compare, for the 'humid' flat plate and the 'humid' cylinder, the averaged rate of evaporation \bar{n}_A obtained by numerically resolving the concentration gradient through the surface, i.e., Eqs. 5-6 with the analytical expressions available for these benchmark cases as given by Eqs. 2-4.

3.1. Benchmark Cases

To evaluate the relations 5-6 used to compute the surface averaged rate of evaporation, we now assess it in comparison with the expression given by the relations (2-4) for both reference geometries, i.e., the flow over the 'wet' flat plate and the flow over the 'wet' cylinder. The numerical domain of such configurations are given in Fig. 4:

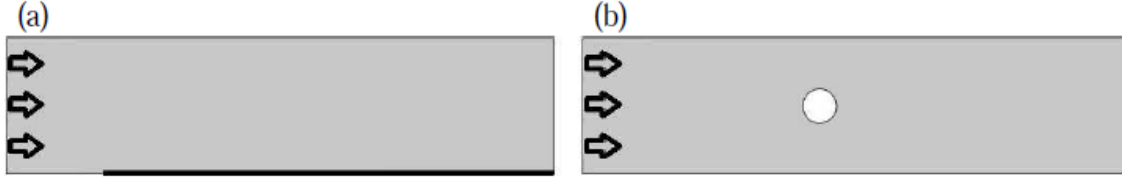


Fig. 4: Benchmark cases: (a) the flow over a ‘wet’ flat plate and (b) the flow over a ‘wet’ cylinder. These cases are used to validate the general approach to compute the rate of evaporation as given by relation 5.

In the numerical modelling of these benchmark cases, both geometries have a saturated concentration of water vapor, computed using expression (1), imposed as a boundary condition. The free stream at the inlet consisted of dry air with a inlet velocity within the range $75 \text{ cm/s} \leq U_{air} \leq 5 \text{ m/s}$ for the flat plate case and $10 \text{ cm/s} \leq U_{air} \leq 1 \text{ m/s}$ for the cylinder geometry. Based on the gradient concentration between the surface and the air flow over it and the associated boundary layer formed in the wall region, the vapor flux driven by relations (5-6) is expected to account for the rate of evaporation, \bar{n}_A , obtained at the ‘wet’ solid surface in similar manner as the rate of evaporation predicted using the relations (2-4). In Fig. 5 the results of \bar{n}_A are show for both geometries.

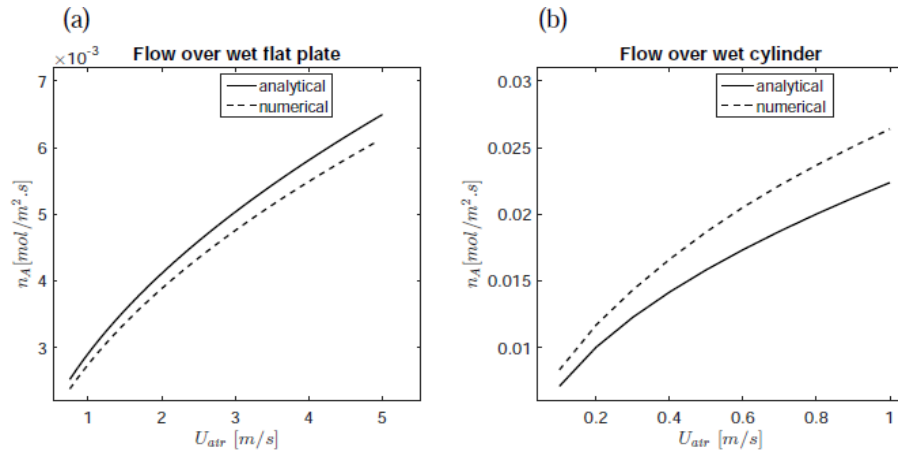


Fig. 5: Results of the rate of evaporation, n_A , as a function of the air free stream speed of (a) the humid flat plate and (b) the humid cylinder. Here, ‘analytical’ refers to the cases where n_A is determined using the relations (2-4) while ‘numerical’ to the cases where the evaporation rate is computer using the expressions (5-6).

In Fig. 6 we define, for comparison purposes, a normalized rate of evaporation, n_A/n_{Amax} , for both benchmark cases. Here, we are interested to check whether the behaviour of the analytical model in terms of the Reynolds number, Re , is obtained in the numerical model. This is needed to describe accurately the dependence of the rate of evaporation as a function of the air flow speed, U_{air} . When we determine the angular coefficient of the linear fit for both geometries we obtain $\alpha = 1.0003$ for the flow over the ‘wet’ flat plate and $\alpha = 1.0075$ for the flow over the ‘wet’ cylinder. These results indicate that, despite the visible magnitude deviation of \bar{n}_A , especially at higher U_{air} as shown in Fig. 5, the same power law dependence in terms of the air speed U_{air} is found in the numerical model when compared to the analytical expressions of \bar{n}_A available for these reference geometries.

In fact, based on this approach one can compute the rate of evaporation along any type of surface when the mass transfer coefficient, h_m , is not promptly available in terms of analytical or empirical expressions. This procedure automatically incorporate the effects of the air flow and of the surface geometry on the rate of evaporation, n_A , thus providing a direct approach to obtain it on any type of surface where a boundary layer develops, as long as the diffusion process is accurately described by a Fick’s law of diffusion. Our problem now reduces to compute the water vapor transport flux along the ‘wetted’ fractal shaped surfaces mentioned in section 2, which we discuss in the next section.

4. Convective Mass and Momentum Transfer in Humid Fractal surfaces

In this paper, our main motivation is to enhance the evaporation of a ‘humid’ surface, i.e., the convective mass transfer, by the application of fractal surfaces on it. We expect that by including fractals on the solid surface then at the same power input, i.e., inlet velocity, a substantial enhancement of the evaporation can be achieved when compared with the case where no-fractals structures are added. However, it is also expected that the inlet pressure will increase due to the imposed multi-scale fractals. Thus, in this section we initially characterize the effects of the imposed fractal forcing on the inlet pressure for this type of flow. We define the fractals surfaces based on the number of iterations carried out to obtain it, thus fractal *Koch-I*, for instance, corresponds to the fractal surface obtained after one iteration and so on.

In Fig. 7 we evaluate the effects of the fractal forcing in the pressure drop, dP , along the flow. Results of dP are obtained considering the averaged pressure drop from the inlet to the outlet region of the numerical

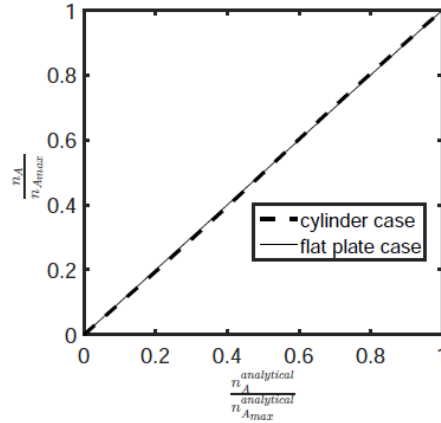


Fig. 6: Results of the normalized rate of evaporation, $\frac{\bar{n}_A}{\bar{n}_{Amax}}$, obtained using the numerical procedure stated in section 3, as a function of the normalized rate of evaporation obtained analytically using the relations given by (2-4). For both benchmark cases there is a full linear correlation between the numerical and the analytical results, thereby indicating that the numerical model captures the same power law dependence of \bar{n}_A in terms of the free stream speed, U_{air} .

domain presented in section 2. For comparison purposes, we normalize the results obtained in the fractal geometries with those obtained in the reference case, i.e., no fractal structures. The results show that for both fractal geometries an increase of the pressure drop occurs relatively to the reference case, as expected, with a substantial increase of the inlet pressure at higher speeds.

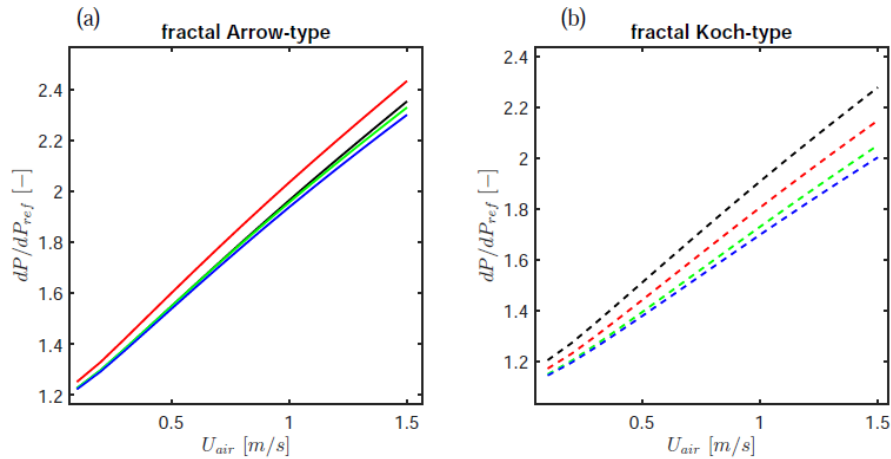


Fig. 7: Results of the pressure drop, dP , as a function of the free stream speed, U_{air} , for all cases with fractals structures imposed. Solid lines corresponds to the results of (a) *arrow*-type fractals and dashed lines to the (b) *Koch*-type cases. Both results are normalized with the pressure drop obtained for the reference case, dP_{ref} . Line colors correspond to fractals generated with one iteration (black), two iterations (red), three iterations (green) and four iterations (blue).

The effects of these fractal structures in the rate of evaporation, \bar{n}_A , are shown in Fig. 8. Clearly, for both cases the self-similarity property of these fractal structures is capable of enhancing significantly the rate of evaporation due to the associated increase of the surface area as the number of iterations to generate the fractal surfaces becomes higher. Since arrow-type geometries have larger surface area, at corresponding iteration level, than the *Koch*-type geometries the enhancement of the rate of evaporation is larger in the former geometries. As can be observed, at lower free stream speeds the case *arrow*-type IV is capable of enhancing the rate of evaporation up to a factor of 3 in comparison with the reference case, while for the case *Koch*-type IV such increase is around of 1.8.

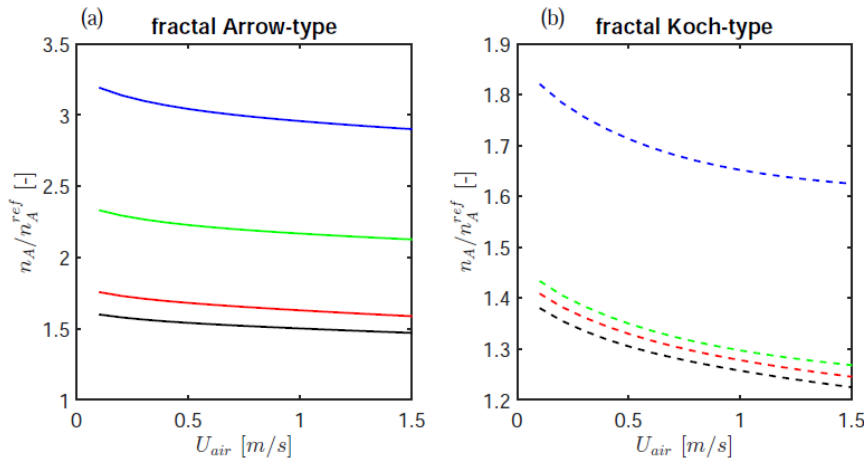


Fig. 8: Results of the rate of evaporation, \bar{n}_A , relatively to the reference case, for all cases investigated. Solid lines correspond to the results of (a) *arrow*-type fractals and dashed lines to the (b) *Koch*-type cases. Line colors correspond to fractals generated with one iteration (black), two iterations (red), three iterations (green) and four iterations (blue).

In order to compare the increase of the inlet pressure, which is an ‘adverse’ effect, and the enhancement of the rate of evaporation, \bar{n}_A , which is our ‘intended’ effect, introduced by imposing these fractal structures, we define a ‘gain’ factor, $f_{gain} = \frac{f_{evap}}{f_{press}}$ where $f_{evap} = \frac{\bar{n}_A}{\bar{n}_A^ref}$ and $f_{press} = \frac{dP}{dP^ref}$, to quantify the advantages of such multi-scale forcing to enhance the convective mass transfer. Whenever $f_{gain} > 1$ then the ‘intended’ effects are achieved otherwise not. The results of $f_{gain} > 1$ associated with the imposed fractals are shown in Fig. 9 for all cases investigated. Clearly, while both fractal geometries show their potential to enhance the mass transfer convection, the fractal geometry *arrow*-type shows to have more versatility within a significant range of flow speeds and a large ‘gain’ factor than the *Koch*-type fractals.

5. Conclusion

A general modelling approach based on commonly adopted assumptions, e.g., thermodynamical equilibrium just above the ‘wetted’ surface in combination with Fick’s law of diffusion, was applied to assess the rate of evaporation, n_A , on any type of complex shaped surface. This procedure was validated in terms of two benchmark cases, e.g., the flow over a flat plate and the flow over a cylinder. Subsequently, we used this model to evaluate the convection mass transfer on ‘wetted’ surfaces with fractal structures superimposed on it. In this paper, several fractal shapes were considered, namely geometries belonging to the *Sierpinski* fractal set and to the *Von Koch* set. The results show that the use of surfaces with fractal structures embedded contributes substantially to the enhancement of the surface averaged rate of evaporation, n_A , due to the inherent capability of these self-similar structures to increase the surface area when compared with surfaces without any fractals on it.

Results for the ‘gain’ factor, f_{gain} , show quantitatively that, although such fractal geometries might lead to an increase of the inlet pressure in the flow, the benefits associated with their introduction to enhance the rate of evaporation are significantly larger. In this paper, the analysis of convective mass transfer was restricted to isothermal cases, thus the subsequent extension of it will include thermal heat transfer associated

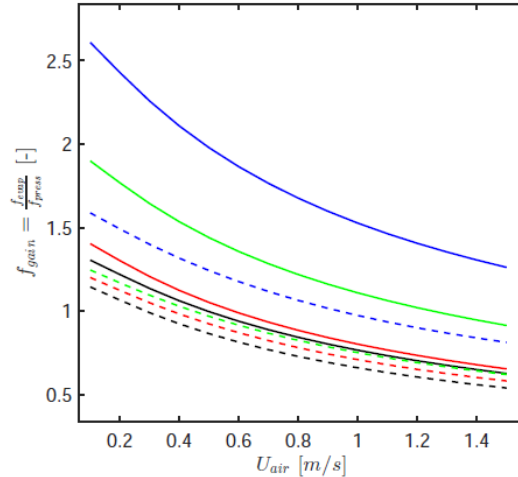


Fig. 9: Results of the ‘gain’ factor, f_{gain} , associated with the applied multi-scale fractal forcing as a function of the free stream speed, U_{air} . Solid lines corresponds to results of the *arrow*-type fractals and the dashed lines to *Koch*-type fractals. Line colors correspond to fractals generated with one iteration (black), two iterations (red), three iterations (green) and four iterations (blue).

with the evaporative cooling. Additionally, the analysis of convection heat-mass transfer in porous medium with fractal surfaces attached to it is of much interest and currently under consideration.

References

- [1] L. Sætran, L. Oggiano, “Skin suit aerodynamics in speed skating,” in *Sport Aerodynamics*, 2008, pp. 93-105, Springer Vienna.
- [2] T. Cardoso de Souza, et al. “Modulation of a methane Bunsen flame by upstream perturbations,” *Journal of Turbulence*, vol. 18, no. 4, pp. 316-337, 2017.
- [3] A. A. Verbeek, T. W. F. M. Bouten, G. G. M. Stoffels, B. J. Geurts, T. H. van der Meer, “Fractal turbulence enhancing low-swirl combustion,” *Combustion and Flame*, vol. 162, no. 1, pp. 129-143, 2015.
- [4] J. Nedic, et al, “Aeroacoustic performance of fractal spoilers,” *Aiaa Journal*, vol. 50, no. 12, pp. 2695- 2710, 2012.
- [5] B. Mazzi, J. C. Vassilicos, “Fractal-generated turbulence,” *Journal of Fluid Mechanics*, vol. 502, pp. 65-87, 2004.
- [6] P. S. Addison, “*Fractals and chaos: an illustrated course*,” CRC Press, 1997.
- [7] B. B. Mandelbrot, R. Pignoni, “*The fractal geometry of nature*,” WH freeman New York, 1983.
- [8] T. L. Bergman, F. P. Incropera, D. P. DeWitt, A. S. Lavine, “*Fundamentals of heat and mass transfer*,” John Wiley & Sons, 2011.